Multi-Object Representation Learning with Iterative Variational Inference

Klaus Greff [1 2] **Raphaël Lopez Kaufman** [3] **Rishabh Kabra** [3] **Nick Watters** [3] **Chris Burgess** [3] **Daniel Zoran** [3]
Loic Matthey [3] **Matthew Botvinick** [3] **Alexander Lerchner** [3]

Abstract

Human perception is structured around objects which form the basis for our higher-level cognition and impressive systematic generalization abilities. Yet most work on representation learning focuses on feature learning without even considering multiple objects, or treats segmentation as an (often supervised) preprocessing step. Instead, we argue for the importance of learning to segment and represent objects *jointly*. We demonstrate that, starting from the simple assumption that a scene is composed of multiple entities, it is possible to learn to segment images into interpretable objects with disentangled representations. Our method learns – without supervision – to inpaint occluded parts, and extrapolates to scenes with more objects and to unseen objects with novel feature combinations. We also show that, due to the use of iterative variational inference, our system is able to learn multi-modal posteriors for ambiguous inputs and extends naturally to sequences.

1. Introduction

Learning good representations of complex visual scenes is a challenging problem for artificial intelligence that is far from solved. Recent breakthroughs in unsupervised representation learning (Higgins et al., 2017a; Makhzani et al., 2015; Chen et al., 2016) tend to focus on data where a single object of interest is placed in front of some background (e.g. dSprites, 3D Chairs, CelebA). Yet in general, visual scenes contain a variable number of objects arranged in various spatial configurations, and often with partial occlusions (e.g., CLEVR, Johnson et al. 2017; see Figure 1). This motivates the question: what forms a good representation of a scene with multiple objects? In line with recent advances (Burgess et al., 2019; van Steenkiste et al., 2018; Eslami et al., 2016), we maintain that discovery of objects in a scene should be considered a crucial aspect of representation learning, rather than treated as a separate problem.

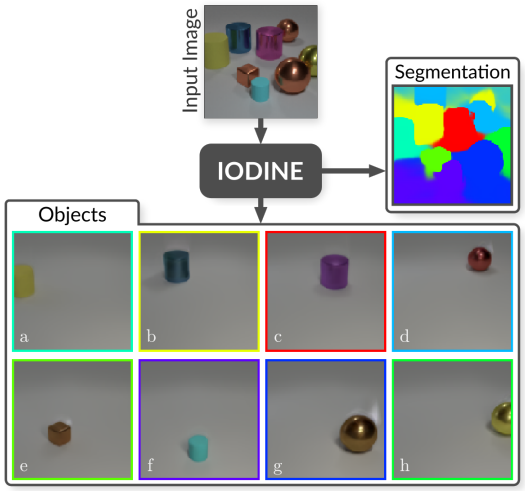

Figure 1. Object decomposition of an image from the CLEVR dataset by IODINE. The model is able to decompose the image into separate objects in an unsupervised manner, inpainting occluded objects in the process (see slots (d), (e) and (h)).

We approach the problem from a spatial mixture model perspective (Greff et al., 2017) and use amortized iterative refinement (Marino et al., 2018b) of latent object representations within a variational framework (Rezende et al., 2014; Kingma & Welling, 2013). We encode our basic intuition about the existence of objects into the structure of our model, which simultaneously facilitates their discovery and efficient representation in a fully data-driven, unsupervised manner. We name the resulting architecture **IODINE** (short for Iterative Object Decomposition Inference NEtwork).

IODINE can segment complex scenes and learn disentangled object features without supervision on datasets like CLEVR, Objects Room (Burgess et al., 2019), and Tetris (see Appendix B). We show systematic generalization to more objects than included in the training regime, as well as objects formed with unseen feature combinations. This highlights the benefits of multi-object representation learning by comparison to a VAE's single-slot representations. We also justify how the sampling used in iterative refinement lends to resolving multi-modal and multi-stable decomposition.

[1]The Swiss AI lab IDSIA, Lugano, Switzerland [2]Work done at DeepMind [3]DeepMind, London, UK. Correspondence to: Klaus Greff <klaus.greff@startmail.com>.

Proceedings of the 36^{th} International Conference on Machine Learning, Long Beach, California, PMLR 97, 2019.

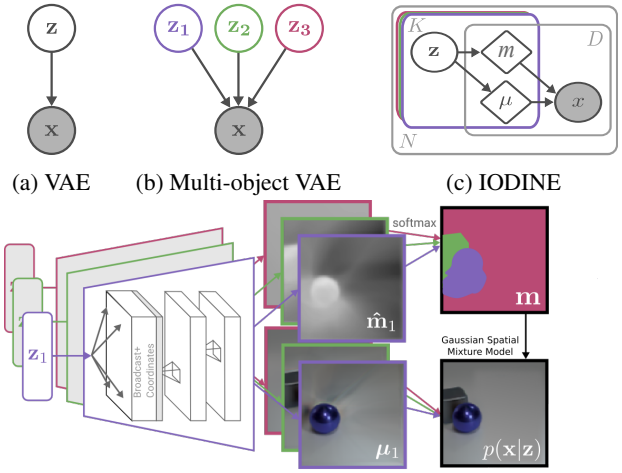

(a) VAE (b) Multi-object VAE (c) IODINE

(d) IODINE neural architecture.

Figure 2. Generative model illustrations. (a) A regular VAE decoder. (b) A hypothetical multi-object VAE decoder that recomposes the scene from three objects. (c) IODINE's multi-object decoder showing latent vectors (denoted $\boldsymbol{z}$) corresponding to K objects refined over N iterations from images of dimension D. The deterministic pixel-wise means and masks are denoted $\boldsymbol{\mu}$ and $\mathbf{m}$ respectively. (d) The neural architecture of the IODINE's multi-object spatial mixture decoder.

2. Method

We first express multi-object representation learning within the framework of generative modelling (Section 2.1). Then, building upon the successful Variational AutoEncoder framework (VAEs; Rezende et al. 2014; Kingma & Welling 2013), we leverage variational inference to jointly learn both the generative and inference model (Section 2.2). There we also discuss the particular challenges that arise for inference in a multi-object context and show how they can be solved using iterative amortization. Finally, in Section 2.3 we bring all elements together and show how the complete system can be trained end-to-end.

2.1. Multi-Object Representations

Flat vector representations as used by standard VAEs are inadequate for capturing the combinatorial object structure that many datasets exhibit. To achieve the kind of systematic generalization that is so natural for humans, we propose employing a *multi-slot* representation where each slot shares the underlying representation format, and each would ideally describe an independent part of the input. Consider the example in Figure 1: by construction, the scene consists of 8 objects, each with its own properties such as shape, size, position, color and material. To split objects, a flat representation would have to represent each object using separate feature dimensions. But this neglects the simple and (to us) trivial fact that they are interchangeable objects with common properties.

Generative Model We represent each scene with K latent object representations $\mathbf{z}_k \in \mathbb{R}^M$ that collaborate to generate the input image $\mathbf{x} \in \mathbb{R}^D$ (c.f. Figure 2b). The $\mathbf{z}_k$ are assumed to be independent and their generative mechanism is shared such that any ordering of them produces the same image (i.e. entailing permutation invariance). Objects distinguished in this way can easily be compared, reused and recombined, thus facilitating combinatorial generalization.

The image $\mathbf{x}$ is modeled with a spatial Gaussian mixture model where each mixing component (slot) corresponds to a single object. That means each object vector $\mathbf{z}_k$ is decoded into a pixel-wise mean μ_{ik} (the appearance of the object) and a pixel-wise assignment $m_{ik} = p(C = k|\mathbf{z}_k)$ (the segmentation mask; c.f. Figure 2c). Assuming that the pixels i are independent conditioned on $\mathbf{z}$, the likelihood thus becomes:

$$p(\mathbf{x}|\mathbf{z}) = \prod_{i=1}^{D} \sum_{k=1}^{K} m_{ik} \mathcal{N}(x_i; \mu_{ik}, \sigma^2), \tag{1}$$

where we use a global fixed variance σ^2 for all pixels.

Decoder Structure Our decoder network structure directly reflects the structure of the generative model. See Figure 2d for an illustration. Each object latent $\mathbf{z}_k$ is decoded separately into pixel-wise means $\boldsymbol{\mu}_k$ and mask-logits $\hat{\mathbf{m}}_k$, which we then normalize using a softmax operation applied across slots such that the masks $\mathbf{m}_k$ for each pixel sum to 1. Together, $\boldsymbol{\mu}$ and $\mathbf{m}$ parameterize the spatial mixture distribution as defined in Equation (1). For the network architecture we use a broadcast decoder (Watters et al., 2019), which spatially replicates the latent vector $\mathbf{z}_k$, appends two coordinate channels (ranging from -1 to 1 horizontally and vertically), and applies a series of size-preserving convolutional layers. This structure encourages disentangling the position across the image from other features such as color or texture, and generally supports disentangling. All slots k share weights to ensure a common format, and are independently decoded, up until the mask normalization.

2.2. Inference

Similar to VAEs, we use amortized variational inference to get an approximate posterior $q_\lambda(\mathbf{z}|\mathbf{x})$ parameterized as a Gaussian with parameters $\boldsymbol{\lambda} = \{\boldsymbol{\mu}_{\boldsymbol{z}}, \boldsymbol{\sigma}_{\boldsymbol{z}}\}$. However, our object-oriented generative model poses a few specific challenges for the inference process: Firstly, being a (spatial) mixture model, we need to infer both the components (i.e. object appearance) and the mixing (i.e. object segmentation). This type of problem is well known, for example in clustering and image segmentation, and is traditionally tackled as an iterative procedure, because there are no efficient direct solutions. A related second problem is that any slot can, in principle, explain any pixel. Once a pixel is explained

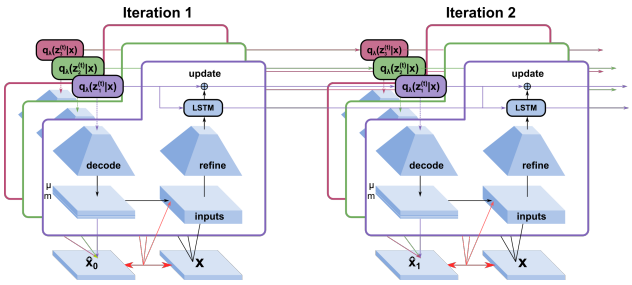

Figure 3. Illustration of the iterative inference procedure.

by one of the slots, the others don't need to account for it anymore. This explaining-away property complicates the inference by strongly coupling it across the individual slots. Finally, slot permutation invariance induces a multimodal posterior with at least one mode per slot permutation. This is problematic, since our approximate posterior $q_\lambda(\mathbf{z}|\mathbf{x})$ is parameterized as a unimodal distribution. For all the above reasons, the standard feed-forward VAE inference model is inadequate for our case, so we consider a more powerful method for inference.

Iterative Inference The basic idea of iterative inference is to start with an arbitrary guess for the posterior parameters $\boldsymbol{\lambda}$, and then iteratively refine them using the input and samples from the current posterior estimate. We build on the framework of iterative amortized inference (Marino et al., 2018b), which uses a trained refinement network f_ϕ. Unlike Marino et al., we consider only additive updates to the posterior and use several salient auxiliary inputs $\mathbf{a}$ to the refinement network (instead of just $\nabla_\lambda \mathcal{L}$). We update the posterior of the K slots independently and in parallel (indicated by $\overset{k}{\leftarrow}$ and $\overset{k}{\sim}$), as follows:

$$\mathbf{z}_k^{(t)} \overset{k}{\sim} q_\lambda(\mathbf{z}_k^{(t)}|\mathbf{x}) \tag{2}$$

$$\boldsymbol{\lambda}_k^{(t+1)} \overset{k}{\leftarrow} \boldsymbol{\lambda}_k^{(t)} + f_\phi(\mathbf{z}_k^{(t)}, \mathbf{x}, \mathbf{a}_k)\,, \tag{3}$$

Thus the only place where the slots interact are at the input level. As refinement network f_ϕ we use a convolutional network followed by an LSTM (see Appendix C for details). Instead of amortizing the posterior directly (as in a regular VAE encoder), the refinement network can be thought of as amortizing the gradient of the posterior (Marino et al., 2018a). The alternating updates to $q_\lambda(\mathbf{z}|\mathbf{x})$ and $p(\mathbf{x}|\mathbf{z})$ are also akin to message passing.

Inputs For each slot k we feed a set of auxiliary inputs $\boldsymbol{a}_k$ to the refinement network f_ϕ which then computes an update for the posterior $\boldsymbol{\lambda}_k$. Crucially, we include gradient information about the ELBO in the inputs, as it conveys information about what is not yet explained by other slots. Omitting the superscript (t) for clarity, the auxiliary inputs $\mathbf{a}_k$ are (see Appendix C for details): image $\mathbf{x}$, means $\boldsymbol{\mu}_k$, masks $\mathbf{m}_k$, mask-logits $\hat{\boldsymbol{m}}_k$, mean gradient $\nabla_{\boldsymbol{\mu}_k}\mathcal{L}$, mask gradient $\nabla_{\mathbf{m}_k}\mathcal{L}$, posterior gradient $\nabla_{\boldsymbol{\lambda}_k}\mathcal{L}$, posterior mask $p(\mathbf{m}_k|\mathbf{x}, \boldsymbol{\mu}) = \frac{p(x|\mu_k)}{\sum_j p(x|\mu_j)}$, pixelwise likelihood $p(\mathbf{x}|\mathbf{z})$, leave-one-out likelihood $p(\mathbf{x}|\mathbf{z}_{i\neq k})$, and two coordinate channels like in the decoder.

Algorithm 1 IODINE Pseudocode.

Input: image $\mathbf{x}$, hyperparamters K, T, σ^2
Input: trainable parameters $\boldsymbol{\lambda}^{(1)}$, $\boldsymbol{\theta}$, $\boldsymbol{\phi}$
Initialize: $\mathbf{h}_k^{(1)} \overset{k}{\leftarrow} \mathbf{0}$
for $t = 1$ **to** T **do**
  $\mathbf{z}_k^{(t)} \overset{k}{\sim} q_\lambda(\mathbf{z}_k^{(t)}|\mathbf{x})$ // Sample
  $\boldsymbol{\mu}_k^{(t)}, \hat{\boldsymbol{m}}_k^{(t)} \overset{k}{\leftarrow} g_\theta(\mathbf{z}_k^{(t)})$ // Decode
  $\boldsymbol{m}^{(t)} \leftarrow \mathrm{softmax}_k(\hat{\boldsymbol{m}}_k^{(t)})$ // Masks
  $p(\mathbf{x}|\mathbf{z}^{(t)}) \leftarrow \sum_k \boldsymbol{m}_k^{(t)} \mathcal{N}(\mathbf{x}; \boldsymbol{\mu}_k^{(t)}, \sigma^2)$ // Likelihood
  $\mathcal{L}^{(t)} \leftarrow D_{KL}(q_\lambda(\mathbf{z}^{(t)}|\mathbf{x})||p(\mathbf{z})) - \log p(\mathbf{x}|\mathbf{z}^{(t)})$
  $\mathbf{a_k} \overset{k}{\leftarrow} \mathrm{inputs}(\mathbf{x}, \mathbf{z}_k^{(t)}, \boldsymbol{\lambda}_k^{(t)})$ // Inputs
  $\boldsymbol{\lambda}_k^{(t+1)}, \mathbf{h}^{(t+1)} \overset{k}{\leftarrow} f_\phi(\mathbf{a}_k, \mathbf{h}_k^{(t)})$ // Refinement
end for

With the exception of $\nabla_{\boldsymbol{\lambda}_k}\mathcal{L}$, these are all image-sized and cheap to compute, so we feed them as additional input-channels into the refinement network. The approximate gradient $\nabla_{\boldsymbol{\lambda}_k}\mathcal{L}$ is computed using the reparameterization trick by a backward pass through the generator network. This is computationally quite expensive, but we found that this information helps to significantly improve training of the refinement network. This input is the same size as the posterior $\boldsymbol{\lambda}_k$ and is fed to the LSTM part of the refinement network. Like Marino et al. (2018b) we found it beneficial to normalize the gradient-based inputs with LayerNorm (Ba et al., 2016). See Section 4.3 for an ablation study.

2.3. Training

We train the parameters of the decoder ($\boldsymbol{\theta}$), of the refinement network ($\boldsymbol{\phi}$), and of the initial posterior ($\boldsymbol{\lambda}^{(1)}$) by gradient descent through the unrolled iterations. In principle, it is enough to minimize the final negative ELBO $\mathcal{L}^T$, but we found it beneficial to use a weighted sum which also includes earlier terms:

$$\mathcal{L}_{\text{total}} = \sum_{t=1}^{T} \frac{t}{T} \mathcal{L}^{(t)}. \tag{4}$$

Each refinement step of IODINE uses gradient information to optimize the posterior $\boldsymbol{\lambda}$. Unfortunately, backpropagating through this process leads to numerical instabilities connected to double derivatives like $\nabla_\Theta \nabla_z \mathcal{L}$. We found that this problem can be mitigated by dropping the double derivative terms, i.e. stopping the gradients from backpropagating through the gradient-inputs $\nabla_{\boldsymbol{\mu}_k}\mathcal{L}$, $\nabla_{\mathbf{m}_k}\mathcal{L}$, and $\nabla_{\boldsymbol{\lambda}_k}\mathcal{L}$ (see Appendix C for details).

3. Related Work

Representation learning (Bengio et al., 2013) has received much attention and has seen several recent breakthroughs. This includes disentangled representations through the use of β-VAEs (Higgins et al., 2017a), adversarial autoencoders (Makhzani et al., 2015), Factor VAEs (Kim & Mnih, 2018), and improved generalization through non-euclidean embeddings (Nickel & Kiela, 2017). However, most advances have focused on the feature-level structure of representations, and do not address the issue of representing multiple, potentially repeating objects, which we tackle here.

Another line of work is concerned with obtaining segmentations of images, usually without considering representation learning. This has led to impressive results on real-world images, however, many approaches (such as "semantic segmentation" or object detection) rely on supervised signals (Girshick, 2015; He et al., 2017; Redmon & Farhadi, 2018), while others require hand-engineered features (Shi & Malik, 2000; Felzenszwalb & Huttenlocher, 2004). In contrast, as we learn to both segment and represent, our method can perform inpainting (Figure 1) and deal with ambiguity (Figure 10), going beyond what most methods relying on feature engineering are currently able to do.

Works tackling the full problem of scene representation are rarer. Probabilistic programming based approaches, like stroke-based character generation (Lake et al., 2015) or 3D indoor scene rendering (Pero et al., 2012), have produced appealing results, but require carefully engineered generative models, which are typically not fully learned from data. Work on end-to-end models has shown promise in using autoregressive inference or generative approaches (Eslami et al., 2016; Gregor et al., 2015), including the recent MONet (Burgess et al., 2019). Few methods can achieve similar comparable with the complexity of the scenes we consider here, apart from MONet. Section 4.1 shows a preliminary comparison between MONet and IODINE, and we discuss their relationship further in Appendix A.3.

Two other methods related to ours are Neural Expectation Maximization (Greff et al., 2017) (along with its sequential and relational extensions (van Steenkiste et al., 2018)) and Tagger (Greff et al., 2016). NEM uses recurrent neural networks to amortize expectation maximization for a spatial mixture model. However, NEM variants fail to cope with colored scenes, as we note in our comparison in Section 4.1. Tagger also uses iterative inference to segment and represent images based on a denoising training objective. We disregard Tagger for our comparison, because (1) its use of a Ladder network means that there is no bottleneck and thus no explicit object representations, and (2) without adapting it to a convolutional architecture, it does not scale to larger images (Tagger would require $\approx$ 600M weights for CLEVR).

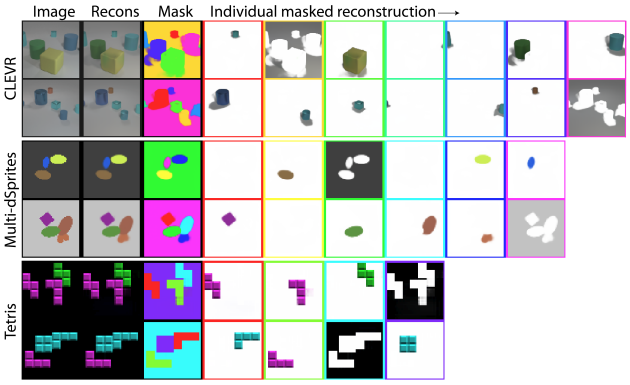

Figure 4. IODINE segmentations and object reconstructions on CLEVR6 (top), Multi-dSprites (middle), and Tetris (bottom). The individual masked reconstruction slots represent objects separately (along with their shadow on CLEVR). Border colours are matched to the segmentation mask on the left.

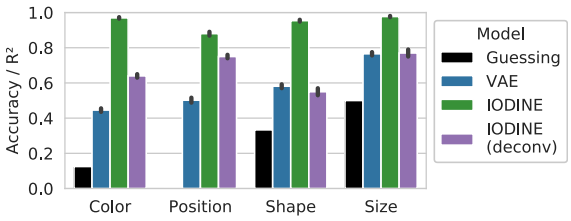

Figure 5. Prediction accuracy / R^2 score for the factor regression on CLEVR6. Position is continuous; the rest are categorical with 8 colors, 3 shapes, and 2 sizes. IODINE (deconv) does not use spatial broadcasting in the decoder (see Section 4.3).

4. Results

We evaluate our model on three main datasets: 1) CLEVR (Johnson et al., 2017) and a variant CLEVR6 which uses only scenes with up to 6 objects, 2) a multi-object version of the dSprites dataset (Matthey et al., 2017), and 3) a dataset of multiple "Tetris"-like pieces that we created. In all cases we train the system using the Adam optimizer (Kingma & Ba, 2015) to minimize the negative ELBO for 10^6 updates. We varied several hyperparameters, including: number of slots, dimensionality of $\mathbf{z}_k$, number of inference iterations, number of convolutional layers and their filter sizes, batch size, and learning rate. For details of the models and hyperparameters refer to Appendix C.

4.1. Decomposition

IODINE can provide a readily interpretable segmentation of the data, as seen in Figure 4. These examples clearly demonstrate the models ability to segmenting out the same objects which were used to generate the dataset, despite never having received supervision to do so. To quantify segmentation quality, we measure the similarity between ground-truth (instance) segmentations and our predicted object masks using the Adjusted Rand Index (ARI; Rand 1971; Hubert & Arabie 1985). ARI is a measure of clustering sim-

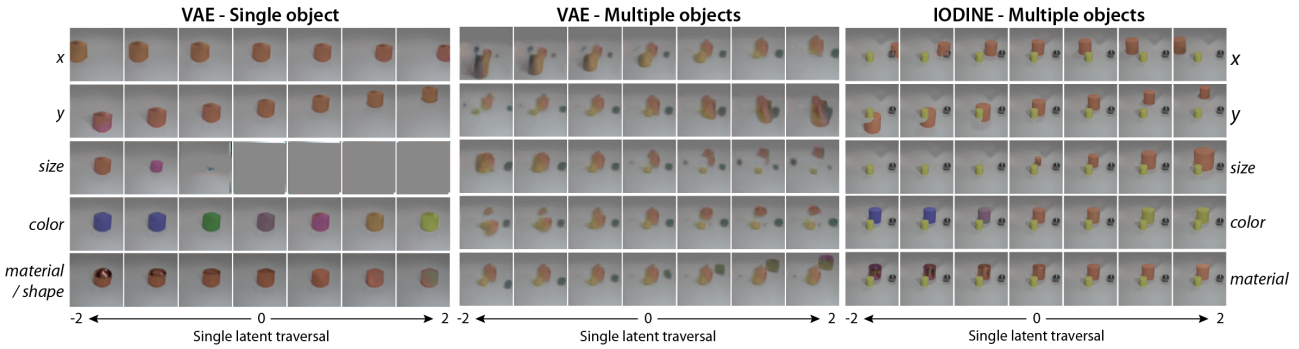

Figure 6. Disentanglement in regular VAEs vs IODINE. Rows indicate traversals of single latents, annotated by our interpretation of their effects. (Left) When a VAE is trained on single-object scenes it can disentangle meaningful factors of variation. (Center) When the same VAE is trained on multi-object scenes, the latents entangle across both factors and objects. (Right) In contrast, traversals of individual latents in IODINE vary individual factors of single objects, here the orange cylinder. Thus, the architectural bias for discovering multiple entities in a common format enables not only the discovery of objects, but also facilitates disentangling of their features.

ilarity that ranges from 0 (chance) to 1 (perfect clustering) and can handle arbitrary permutations of the clusters. We apply it as a measure of instance segmentation quality by treating each foreground pixel (ignoring the background) as one point and its segmentation as cluster assignment. As shown in Table 1, IODINE achieves almost perfect ARI scores of around 0.99 for CLEVR6, and Tetris as well as a relatively good score of 0.77 for Multi-dSprites. The lower scores on Multi-dSprites are largely because IODINE struggles to produce sharp boundaries for the sprites, and we are uncertain as to the reasons for this behaviour.

We compare with MONet (Burgess et al., 2019), following the CLEVR model implementation described in the paper except using fewer (7) slots and different standard deviations for the decoder distribution (0.06 and 0.1 for σ_{bg} and σ_{fg}, respectively), which gave better scores. With this, MONet obtained a similar ARI score (0.96) as IODINE on CLEVR6, and on Multi-dSprites it performed significantly better with a score of 0.90 (using the unmodified model). We also attempted to compare ARI scores to Neural Expectation Maximization, but neither Relational-NEM nor the simpler RNN-NEM variant could cope well with colored images. As a result, we could only compare with those methods on a binarized version of Multi-dSprites and the Shapes dataset. These scores are summarized in Table 1.

	IODINE	R-NEM	MONet
CLEVR6	0.988 ± 0.000	$*$	0.962 ± 0.006
M-dSprites	0.767 ± 0.056	$*$	0.904 ± 0.008
M-dSprites bin.	0.648 ± 0.172	0.685 ± 0.017	
Shapes	0.910 ± 0.119	0.776 ± 0.019	
Tetris	0.992 ± 0.004	$*$	

Table 1. Summary of IODINE's segmentation performance in terms of ARI (mean $\pm$ stddev across five seeds) versus baseline models. For each independent run, we computed the ARI score over 320 images, using only foreground pixels. We then picked the best hyperparameter combination for each model according to the mean ARI score over five random seeds.

4.2. Representation Quality

Information Content The object-reconstructions in Figure 4 show that their representations contain all the information about the object. But in what format, and how usable is it? To answer this question we associate each ground-truth object with its corresponding $\mathbf{z}_k$ based on the segmentation masks. We then train a single-layer network to predict ground-truth factors for each object. Note that this predictor is trained *after* IODINE has finished training (i.e. no supervised fine-tuning). It tells us if a linear mapping is sufficient to extract information like color, position, shape or size of an object from its latent representation, and gives an important indication about the usefulness of the representation. Results in Figure 5 clearly show that a linear mapping is sufficient to extract relevant information about these object attributes from the latent representation to high accuracy. This result is in contrast with the scene representations learned by a standard VAE. Here even training the factor-predictor is difficult, as there is no obvious way to align objects with features. To make this comparison, we chose a canonical ordering of the objects based on their size, material, shape, and position (with decreasing precedence). The precedence of features was intended as a heuristic to maximize the predictability of the ordering. We then trained a linear network to predict the concatenated features of the canonically ordered objects from the latent scene representation. As the results in Figure 5 indicate, the information is present, but in a much less explicit/usable state.

Disentanglement Disentanglement is another important desirable property of representations (Bengio et al., 2013) that captures how well learned features separate and correspond to individual, interpretable factors of variation in the data. While its precise definition is still highly debated (Higgins et al., 2018; Eastwood & Williams, 2018; Ridgeway

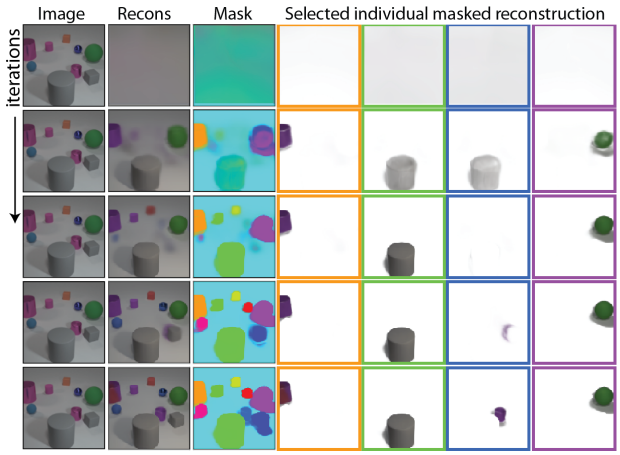

Figure 7. IODINE's iterative inference process and generalization capabilities. Rows indicate steps of iterative inference, refining reconstructions and segmentations when moving down the figure. Of particular interest is the *explaining away* effect visible between slots 2 and 3, where they settle on different objects despite both starting with the large cylinder. The model was only trained with $K = 7$ slots on 3-6 objects (excluding green spheres), and yet is able to generalize to $K = 11$ slots (only 4 are shown, see Figure 19 in the appendix for a full version) on a scene with 9 objects, including the never seen before green sphere (last column).

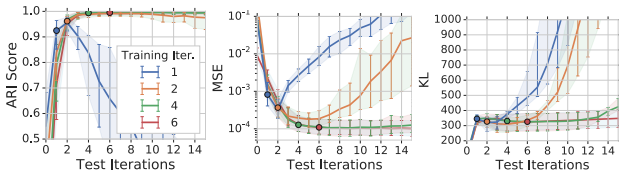

(a) ARI (b) MSE (c) KL

Figure 8. The effect of varying the number of iterations, for both training and at test time. (a) Median ARI score, (b) MSE and (c) KL over test-iterations, for models trained with different numbers of iterations on CLEVR6. The region beyond the filled dots thus shows test-time generalization behavior. Shaded region from 25th to 75th percentile.

& Mozer, 2018; Locatello et al., 2018), the concept of disentanglement has generated a lot of interest recently. Good disentanglement is believed to lead to both better generalization and more interpretable features (Lake et al., 2016; Higgins et al., 2017b). Interestingly, for these desirable advantages to bear out, disentangled features seem to be most useful for properties of single objects, such as color, position, shape, etc. It is much less clear how to operationalize this in order to create disentangled representations of entire scenes with variable numbers of objects. And indeed, if we train a VAE that can successfully disentangle features of a single-object dataset, we find that that its representation becomes highly entangled on a multi-object dataset, (see Figure 6 left vs middle). IODINE, on the other hand, successfully learns disentangled representations, because it is able to first decompose the scene and then represent individual objects (Figure 6 right). In Figure 6 we show traversals of the most important features (selected by KL) of a standard VAE vs IODINE. While the standard VAE clearly entangles many properties even across multiple objects, IODINE is able to neatly separate them.

Generalization Finally, we can ask directly: Does the system generalize to novel scenes in a systematic way? Specifically, does it generalize to scenes with more or fewer objects than ever encountered during training? Slots are exchangeable by design, so we can freely vary the number of slots during test-time (more on this in Section 4.3). So in Figure 7 we qualitatively show the performance of a system that was trained with $K = 7$ on up to 6 objects, but evaluated with $K = 11$ on 9 objects. In Figure 9a the orange boxes show, that, even quantitatively, the segmentation performance decreases little when generalizing to more objects.

A more extreme form of generalization involves handling unseen feature combinations. To test this we trained our system on a subset of CLEVR that does not contain green spheres (though it does contain spheres and other green objects). And then we tested what the system does when confronted with a green sphere. In Figure 7 it can be seen that IODINE is still able to represent green spheres, despite never having seen this combination during training.

4.3. Robustness & Ablation

Iterations The number of iterations is one of the central hyperparameters to our approach. To investigate its impact, we trained four models with 1, 2, 4 and 6 iterations on CLEVR6, and evaluated them all using 15 iterations (c.f. Figure 8). The first thing to note is that the inference converges very quickly within the first 3-5 iterations after which neither the segmentation nor reconstruction change much. The second important finding is that the system is very stable for much longer than the number of iterations it was trained with. The model even further improves the segmentation and reconstruction when it is run for more iterations, though it eventually starts to diverge after about two to three times the number of training iterations as can be seen with the blue and orange curves in Figure 8.

Slots The other central parameter of IODINE is the number of slots K, as it controls the maximum number of objects the system can separate. It is important to distinguish varying K for training vs varying it at test-time. As can be seen in Figure 9, if the model was trained with sufficiently many slots to fit all objects ($K = 7$, and $K = 9$), then test-time behavior generalizes very well. Typical behavior (not shown) is to leave excess slots empty, and when confronted

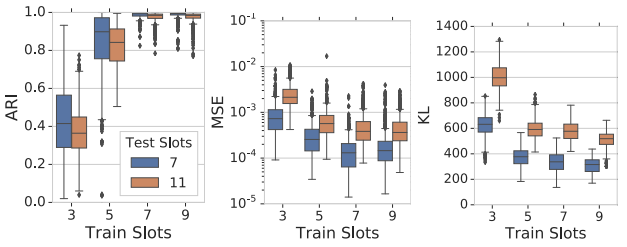

(a) ARI (b) MSE (c) KL

Figure 9. IODINE trained on CLEVR6 with varying numbers of slots (columns). Evaluation of (a) ARI, (b) MSE, and (c) KL with 7 slots on 3-6 Objects (blue) and 11 slots on 3-9 objects (orange).

with too many objects it will often completely ignore some of them, leaving the other object-representations mostly intact. Given enough slots at test time, such a model can even segment and represent scenes of higher complexity (more objects) than any scene encountered during training (see Figure 7 and the orange boxes in Figure 9). If on the other hand, the model was trained with too few slots ($K = 3$ and $K = 5$), its performance suffers substantially. This happens because, here the only way to reconstruct the entire scene during training is to consistently represent multiple objects per slot. And that leads to the model learning inefficient and entangled representations akin to the VAE in Figure 6 (also apparent from their much higher KL in Figure 9c). Once learned, this sub-optimal strategy cannot be mitigated by increasing the number of slots at test-time as can be seen by their decreased performance in Figure 9a.

Input Ablations We ablated each of the different inputs to the refinement network described in Section 2.2. Broadly, we found that individually removing an input did not noticeably affect the results (with two exceptions noted below). See Figures 33-40 in the Appendix demonstrating this lack of effect on different terms of the model's loss and the ARI segmentation score on both CLEVR6 and Tetris. A more comprehensive analysis could ablate combinations of inputs and identify synergistic or redundant groups, and thus potentially simplify the model. We didn't pursue this direction since none of the inputs incurs any noticeable computational overhead and at some point during our experimentation each of them contributed towards stable training behavior.

The main exceptions to the above are $\nabla_\lambda \mathcal{L}$ and $\mathbf{x}$. Computing the former requires an entire backward pass through the decoder, and contributes about 20% of the computational cost of the entire model. But we found that it often substantially improves performance and training convergence, which justifies its inclusion. A somewhat surprising finding was that for the Tetris dataset, removing $\mathbf{x}$ from the list of inputs had a pronounced detrimental effect, while for CLEVR it was negligible.

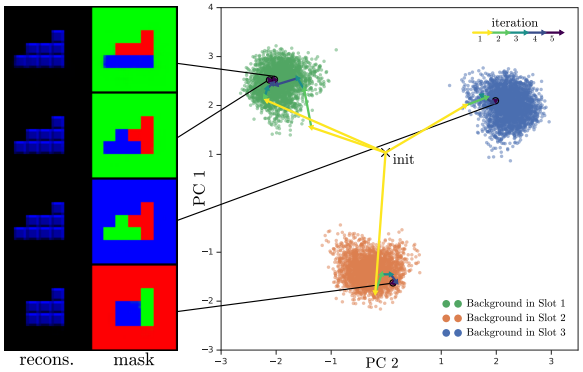

Figure 10. Multi-stability of segmentation when presented with an ambiguous stimulus. **left:** Depending on the random sampling during iterative refinement, IODINE can produce different permutations of groups (row 2 vs 3), a different decomposition (row 1) or sometimes an invalid segmentation and reconstruction (row 4). **right:** PCA of the latent space, coloured by which slot corresponds to the background. Paths show the trajectory of the iterative refinement for the four examples on the left.

Broadcast Decoder Ablation We use the spatial broadcast decoder (Watters et al., 2019) primarily for its significant impact on the disentanglement of the representations, but its continuous spatial representation bias also seems to help decomposition. When replacing it with a deconvolution-based decoder the factor regression scores on CLEVR6 are significantly worse as can be seen in Figure 5. Especially for shape and size it now performs no better than the VAE which uses spatial broadcasting. The foreground-ARI scores also drop significantly (0.67 ± 0.06 down from 0.99) and the model seems less able to specialize slots to single objects (see Figure 23). Note though, that these discrepancies might easily be reduced, since we haven't invested much effort in tuning the architecture of the deconv-based decoder.

4.4. Multi-Modality and Multi-Stability

Standard VAEs are unable to represent multi-modal posteriors, because $q_\lambda(\mathbf{z}|\mathbf{x})$ is parameterized using a unimodal Gaussian distribution. However, as demonstrated in Figure 10, IODINE can actually handle this problem quite well. How is that possible? It turns out that this is an important side-effect of iterative variational inference, that to the best of our knowledge has not been noticed before: The stochasticity at each iteration, which results from sampling $\mathbf{z}$ to approximate the likelihood, implicitly acts as an auxilliary (inference) random variable. This effect compounds over iterations, and is amplified by the slot-structure and the effective message-passing between slots over the course of iterations. In effect the model can implicitly represent multiple modes (if integrated over all ways of sampling $\mathbf{z}$) and thus converge to different modes (see Figure 10 left) depending on these samples. This does not happen in a regular

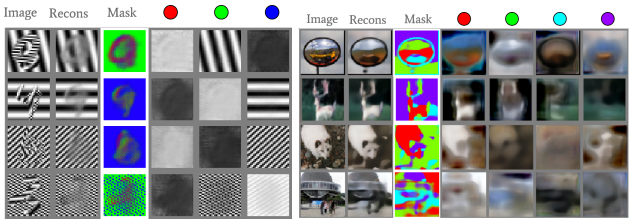

(a) Textured MNIST (b) ImageNet

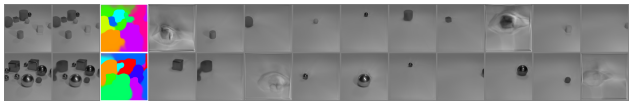

(c) Grayscale CLEVR

Figure 11. Segmentation challenges a) IODINE did not succeed in capturing the foreground digits in the Textured MNIST dataset. b) IODINE groups ImageNet not into meaningful objects but mostly into regions of similar color. c) On a grayscale version of CLEVR, IODINE still produces the desired groupings.

VAE, where no stochasticity enters the inference process. If we had an exact and deterministic way to compute the likelihood and its gradient, this effect would vanish.

A neat side-effect of this is the ability of IODINE to elegantly capture ambiguous (aka multi-stable) segmentations such as the ones shown in Figure 10. We presented the model with an ambiguous arrangement of Tetris blocks, which has three different yet equally valid "explanations" (given the data distribution). When we evaluate an IODINE model on this image, we get different segmentations on different evaluations. Some of these correspond to different slot-orderings (1st vs 3rd row). But we also find qualitatively different segmentations (i.e. 3rd vs 4th row) that correspond to different interpretations of the scene. Multi-stability is a well-studied and pervasive feature of human perception that is important for handling ambiguity, and that not modelled by any of the standard image recognition networks.

5. Discussion and Future Work

We have introduced IODINE, a novel approach for unsupervised representation learning of multi-object scenes, based on amortized iterative refinement of the inferred latent representation. We analyzed IODINE's performance on various datasets, including realistic images containing variable numbers of partially occluded 3D objects, and demonstrated that our method can successfully decompose the scenes into objects and represent each of them in terms of their individual properties such as color, size, and material. IODINE can robustly deal with occlusions by inpainting covered sections, and generalises beyond the training distribution in terms of numerosity and object-property combinations. Furthermore, when applied to scenes with ambiguity in terms of their object decomposition, IODINE can represent – and converge to – multiple valid solutions given the same input image.

We also probed the limits of our current setup by applying IODINE to the Textured MNIST dataset (Greff et al., 2016) and to ImageNet, testing how it would deal with texture-segmentation and more complex real-world data (Figure 11). Trained on ImageNet data, IODINE segmented mostly by color rather than by objects. This behavior is not unexpected: ImageNet was never designed as a dataset for unsupervised learning, and likely lacks the richness in poses, lighting, sizes, positions and distance variations required to learn object segmentations from scratch. Trained on Textured MNIST, IODINE was able to model the background, but mostly failed to capture the foreground digits. Together these results point to the importance of color as a strong cue for segmentation, especially early in the iterative refinement process. As demonstrated by our results on grayscale CLEVR (Figure 11c) though, color is not a requirement.

Beyond more diverse training data, we want to highlight three other promising directions to scale IODINE to richer real-world data. First, an extension to sequential data is attractive, because temporal data naturally contains rich statistics about objectness both in the movement itself, and in the smooth variations of object factors. IODINE can readily be applied to sequences feeding a new frame at every iteration, and we have done some preliminary experiments described in Appendix A.1. As a nice side-effect, the model automatically maintains the object to slot association, turning it into an unsupervised object tracker. However, IODINE in its current form has limited abilities for modelling dynamics.

Physical interaction between objects is another common occurrence in sequential data, which can serve as a strong cue for object decomposition. Similarly even statically placed objects placed commonly adhere to certain relations among each other, such as cars on streets. Currently however, IODINE assumes the objects to be placed independently of each other, and relaxing this assumption will be important for modelling physical interactions. Yet there is also a need to balance this with the independence assumption required to split objects, since the system should still be able to segment out a car floating in space. Thus we believe integration with some form of graph network to support relations while preserving slot symmetry is a promising direction.

Finally, object representations have to be useful, such as for supervised tasks, or for agents in reinforcement learning setups. Whatever the task, it should provide important feedback about which objects matter and which are irrelevant. Complex visual scenes can contain an extremely large number of potential objects (think of sand grains on a beach), which can make it unfeasible to represent them all simultaneously. Thus, allowing task-related signals to bias selection for what and how to decompose, may enable scaling up unsupervised scene representation learning approaches like IODINE to arbitrarily complex scenes.

Acknowledgements

We would like to thank Danilo Rezende, Sjoerd van Steenkiste, and Malcolm Reynolds for helpful suggestions and generous support.

References

Ba, J. L., Kiros, J. R., and Hinton, G. E. Layer normalization. *arXiv:1607. 06450 [cs, stat]*, July 2016.

Bengio, Y., Courville, A., and Vincent, P. Representation learning: A review and new perspectives. *IEEE Trans. Pattern Anal. Mach. Intell.*, 35(8):1798–1828, 2013.

Burgess, C. P., Matthey, L., Watters, N., Kabra, R., Higgins, I., Botvinick, M., and Lerchner, A. MONet: Unsupervised scene decomposition and representation. *arXiv preprint*, January 2019.

Chen, X., Duan, Y., Houthooft, R., Schulman, J., Sutskever, I., and Abbeel, P. InfoGAN: Interpretable representation learning by information maximizing generative adversarial nets. *arXiv:1606.03657 [cs, stat]*, June 2016.

Clevert, D.-A., Unterthiner, T., and Hochreiter, S. Fast and accurate deep network learning by exponential linear units (ELUs). November 2015.

Eastwood, C. and Williams, C. K. I. A framework for the quantitative evaluation of disentangled representations. *ICLR*, 2018.

Eslami, S. M. A., Heess, N., Weber, T., Tassa, Y., Szepesvari, D., Kavukcuoglu, K., and Hinton, G. E. Attend, infer, repeat: Fast scene understanding with generative models. In Lee, D. D., Sugiyama, M., Luxburg, U. V., Guyon, I., and Garnett, R. (eds.), *Advances in Neural Information Processing Systems 29*, pp. 3225–3233. Curran Associates, Inc., 2016.

Felzenszwalb, P. F. and Huttenlocher, D. P. Efficient Graph-Based image segmentation. *Int. J. Comput. Vis.*, 59(2): 167–181, September 2004.

Girshick, R. B. Fast R-CNN. *CoRR*, abs/1504.08083, 2015. URL http://arxiv.org/abs/1504.08083.

Greff, K., Rasmus, A., Berglund, M., Hao, T. H., Valpola, H., and Schmidhuber, J. Tagger: Deep unsupervised perceptual grouping. In Lee, D. D., Sugiyama, M., Luxburg, U. V., Guyon, I., and Garnett, R. (eds.), *Advances in Neural Information Processing Systems 29*, pp. 4484–4492, 2016.

Greff, K., van Steenkiste, S., and Schmidhuber, J. Neural expectation maximization. In Guyon, I., Luxburg, U. V., Bengio, S., Wallach, H., Fergus, R., Vishwanathan, S., and Garnett, R. (eds.), *Advances in Neural Information Processing Systems 30*, pp. 6694–6704. Curran Associates, Inc., 2017.

Gregor, K., Danihelka, I., Graves, A., Rezende, D. J., and Wierstra, D. DRAW: A recurrent neural network for image generation. In *Proceedings of the 32Nd International Conference on International Conference on Machine Learning - Volume 37*, ICML'15, pp. 1462–1471, Lille, France, 2015. JMLR.org.

He, K., Gkioxari, G., Dollár, P., and Girshick, R. B. Mask R-CNN. *CoRR*, abs/1703.06870, 2017. URL http://arxiv.org/abs/1703.06870.

Higgins, I., Matthey, L., Pal, A., Burgess, C., Glorot, X., Botvinick, M., Mohamed, S., and Lerchner, A. beta-VAE: Learning basic visual concepts with a constrained variational framework. In *In Proceedings of the International Conference on Learning Representations (ICLR)*, 2017a.

Higgins, I., Pal, A., Rusu, A., Matthey, L., Burgess, C., Pritzel, A., Botvinick, M., Blundell, C., and Lerchner, A. DARLA: Improving zero-shot transfer in reinforcement learning. *ICML*, 2017b.

Higgins, I., Amos, D., Pfau, D., Racanière, S., Matthey, L., Rezende, D. J., and Lerchner, A. Towards a definition of disentangled representations. *CoRR*, abs/1812.02230, 2018. URL http://arxiv.org/abs/1812.02230.

Hubert, L. and Arabie, P. Comparing partitions. *J. Classification*, 2(1):193–218, December 1985.

Johnson, J., Hariharan, B., van der Maaten, L., Fei-Fei, L., Zitnick, C. L., and Girshick, R. CLEVR: A diagnostic dataset for compositional language and elementary visual reasoning. In *Computer Vision and Pattern Recognition (CVPR), 2017 IEEE Conference on*, pp. 1988–1997. openaccess.thecvf.com, 2017.

Kim, H. and Mnih, A. Disentangling by factorising. February 2018.

Kingma, D. and Ba, J. Adam: A method for stochastic optimization. CBLS, 2015.

Kingma, D. P. and Welling, M. Auto-encoding variational bayes. *arXiv preprint arXiv:1312.6114*, 2013.

Lake, B. M., Salakhutdinov, R., and Tenenbaum, J. B. Human-level concept learning through probabilistic program induction. *Science*, 350(6266):1332–1338, December 2015.

Lake, B. M., Ullman, T. D., Tenenbaum, J. B., and Gershman, S. J. Building machines that learn and think like people. *Behavioral and Brain Sciences*, pp. 1–101, 2016.

Locatello, F., Bauer, S., Lucic, M., Gelly, S., Schölkopf, B., and Bachem, O. Challenging common assumptions in the unsupervised learning of disentangled representations. *arXiv preprint arXiv:1811.12359*, 2018.

Maaten, L. v. d. and Hinton, G. Visualizing data using t-sne. *Journal of machine learning research*, 9(Nov): 2579–2605, 2008.

Makhzani, A., Shlens, J., Jaitly, N., Goodfellow, I., and Frey, B. Adversarial autoencoders. November 2015.

Marino, J., Cvitkovic, M., and Yue, Y. A general method for amortizing variational filtering. In Bengio, S., Wallach, H., Larochelle, H., Grauman, K., Cesa-Bianchi, N., and Garnett, R. (eds.), *Advances in Neural Information Processing Systems 31*, pp. 7868–7879. Curran Associates, Inc., 2018a.

Marino, J., Yue, Y., and Mandt, S. Iterative amortized inference. In Dy, J. and Krause, A. (eds.), *Proceedings of the 35th International Conference on Machine Learning*, volume 80 of *Proceedings of Machine Learning Research*, pp. 3403–3412, Stockholmsmässan, Stockholm Sweden, 2018b. PMLR.

Matthey, L., Higgins, I., Hassabis, D., and Lerchner, A. dsprites: Disentanglement testing sprites dataset. https://github.com/deepmind/dsprites-dataset/, 2017.

Nickel, M. and Kiela, D. Poincaré embeddings for learning hierarchical representations. In Guyon, I., Luxburg, U. V., Bengio, S., Wallach, H., Fergus, R., Vishwanathan, S., and Garnett, R. (eds.), *Advances in Neural Information Processing Systems 30*, pp. 6338–6347. Curran Associates, Inc., 2017.

Pascanu, R., Mikolov, T., and Bengio, Y. Understanding the exploding gradient problem. *CoRR, abs/1211. 5063*, 2012.

Pero, L. D., Bowdish, J., Fried, D., Kermgard, B., Hartley, E., and Barnard, K. Bayesian geometric modeling of indoor scenes. In *2012 IEEE Conference on Computer Vision and Pattern Recognition*, pp. 2719–2726. ieeexplore.ieee.org, June 2012.

Rand, W. M. Objective criteria for the evaluation of clustering methods. *J. Am. Stat. Assoc.*, 66(336):846–850, December 1971.

Redmon, J. and Farhadi, A. Yolov3: An incremental improvement. *CoRR*, abs/1804.02767, 2018. URL http://arxiv.org/abs/1804.02767.

Reichert, D. P. and Serre, T. Neuronal Synchrony in Complex-Valued Deep Networks. *arXiv:1312. 6115 [cs, q-bio, stat]*, December 2013.

Rezende, D. J., Mohamed, S., and Wierstra, D. Stochastic backpropagation and approximate inference in deep generative models. In Xing, E. P. and Jebara, T. (eds.), *Proceedings of the 31st International Conference on Machine Learning*, volume 32 of *Proceedings of Machine Learning Research*, pp. 1278–1286, Bejing, China, 2014. PMLR.

Ridgeway, K. and Mozer, M. C. Learning deep disentangled embeddings with the f-statistic loss. *NIPS*, 2018.

Shi, J. and Malik, J. Normalized cuts and image segmentation. *IEEE Trans. Pattern Anal. Mach. Intell.*, 22(8): 888–905, August 2000.

van Steenkiste, S., Chang, M., Greff, K., and Schmidhuber, J. Relational neural expectation maximization: Unsupervised discovery of objects and their interactions. In *Proceedings of the International Conference on Learning Representations (ICLR)*, January 2018.

Watters, N., Matthey, L., Burgess, C. P., and Lerchner, A. Spatial broadcast decoder: A simple architecture for learning disentangled representations in vaes. *arXiv*, 1901.07017, 2019.